High-resolution Urban Thermal Sharpener (HUTS)

Anthony Dominguez[a], Jan Kleissl[a], Jeffrey C. Luvall[b], and Douglas L. Rickman[b]

[a]*University of California, San Diego, Department of Mechanical and Aerospace Engineering*

[b]*NASA, Marshall Space Flight Center, AL 35812, USA*

Corresponding author

Jan Kleissl, jkleissl@ucsd.edu, Office: (858) 534-8087; Fax: (858) 534-7599;

Address: 9500 Gilman Dr, EBUII – 580, University of California, San Diego, La Jolla, CA, 92093

Abstract

A high resolution urban thermal sharpener (HUTS) was developed that increases the resolution of thermal infrared (TIR) data to that of visible and near infrared (VNIR) data by fitting the relationship between radiometric surface temperature, normalized difference vegetation index (NDVI) and surface albedo (α). HUTS was applied to TIR data aggregated to 90 m to represent a satellite acquired dataset and validated against the measured 10 m data from aircraft over San Juan, Puerto Rico. HUTS sharpening reduced the root mean square error of surface temperature at the high resolution by 17 % compared to no sharpening and outperformed other sharpening methods. HUTS is proposed as a useful tool to study urban meteorology and climatology at the microscale using ASTER satellite data.

Keywords

Land surface temperature, Thermal sharpening, Urban heat island, Urban meteorology

1. Introduction

Satellites acquire thermal infrared (TIR) data to compute land surface temperature (LST) at a resolution as high as 60 m (Landsat ETM+). This information can be used to study the impact of urbanization such as the Surface Urban Heat Island (SUHI) which describes the increase in (radiometric) LST in an urban area compared to surrounding rural areas (Voogt and Oke, 2003). UHIs have fundamental impacts on meteorology (e.g. land-sea breezes, Lebassi et al. 2009), air quality, public health (e.g. heat related deaths, Beniston, 2004), energy consumption, and economics. The global coverage of satellites allowed quantifying and studying the SUHI in e.g. Houston, Texas (Streutker 2003), Indianapolis, Indiana (Wilson et al. 2003), and 18 Asian mega cities (Hung et al. 2006). While satellite TIR resolution resolves the scales of urban-rural LST differences, it is not sufficient to resolve most urban features (roads, buildings) to study microclimates and human comfort in urban areas.

As the pace of urbanization increases, studies on the microclimate within urban areas are becoming more important as urban canyon LST affects pedestrian heat stress (Crutzen 2004) and building energy use (Yaghoobian et al. 2010). High resolution TIR data from remote sensors flown on aircraft (e.g. NASA's Advanced Thermal and Land Applications Sensor, ATLAS, 5 m to 10 m resolution, depending on flight altitude) has been used to study the surface microclimate over Huntsville, Alabama (Lo et al. 1997), and generate thermal, land cover classification, and urban fabric maps for Atlanta, Georgia, Baton Rouge, Lousiana, Salt Lake City, Utah, and Sacramento, California (Quattrochi et al. 2000). A one-day intensive experiment was conducted in Phoenix, Arizona using airborne IR thermography to investigate the UHI at

different spatial scales (Di Sabatino et al. 2009). Airborne remote sensing campaigns are limited in spatial extent and repeat cycle due to high cost. As each urban microclimate is unique due to urban fabric and meteorology, a tool that would allow the downscaling of global satellite datasets in urban areas would be extremely useful. The utility of global and repeating high resolution TIR data motivates thermal sharpening, or estimating the TIR data at higher resolution using complementary information available at that resolution.

Visible and Near Infrared (VNIR) data can generally be acquired at higher resolution than TIR as a consequence of their shorter wavelength. Kustas et al. (2003) leveraged higher resolution VNIR data by relating LST to the normalized difference vegetative index (NDVI) at the lower resolution (96 m) and then applying the relation at the higher resolution available for NDVI (24 m). Agam et al. (2007) replaced NDVI by a simplified fractional vegetation cover and named the method TsHARP. TsHARP provided reasonably accurate high resolution (60 m) TIR maps from 1 km TIR data, but the accuracy decreased with increased resolution of the sharpened map (Agam et al., 2008). In urban areas, solar reflectance (albedo) is another determinant of LST. While LST is a function of land class(e.g. deep water and shadowed areas are cooler than equally low-albedo sunlit surfaces) , Small (2006) found that within unshaded land classes albedo correlates well with LST.

Guo and Moore (1998) sharpened LST using the VNIR bands to identify topographic variations. While LST forareas with varied topography and homogeneous land cover where sun angle is the driving force for LST differences can be predicted accurately, this method is not applicable to flat urban areas with very heterogeneous land covers. Nichol (2009) sharpened a

nighttime ASTER image of Hong Kong using emissivities based on land class from the MODIS emissivity library. However, emissivity is not the main determinant of LST during the daytime, and the accuracy of the land class based emissivities is questionable when emissivity libraries are used.

In this study high resolution ATLAS data (Section 2) over urban Puerto Rico is analyzed. Based on the relationship between TIR derived LSTs and VNIR signals (Section 3), a High-resolution Urban Thermal Sharpening method (HUTS) is proposed using *NDVI* and albedo from the VNIR channels (Section 4). The high resolution ATLAS data are used to quantify the accuracy of HUTS and TsHARP (Section 5).

2. ATLAS Airborne Data

NASA ATLAS data taken over the greater San Juan, Puerto Rico area on February 16, 2004 (Gonzalez et al. 2005, 2006) at 10 m resolution over 15 spectral channels (Table 1) is used. The study focuses on a 900 x 720 pixel (9 km x 7.2 km) urban and suburban, cloud-free region from the 3rd flight line at 5200 m altitude, taken between 1507 and 1512 local standard time (AST, Fig. 1). Air temperature on this day averaged 26 ^{o}C with a high of 28.5 ^{o}C and a low of 23 ^{o}C, Humidity was an average of 80%, varying from 59% to 100%. Winds were from the East at an average 4.5 m s^{-1}, but were sustained at 7.6 -9.4 m s^{-1} during 1407-1612 AST (NWS Daily Summary). Since the study area is flat, topographic shading is minimal. Shadows will be present due to (primarily low) buildings and the early afternoon flight time. Considering solar geometry at the time of the flight, the shadow length for a 3 m tall building would be 2.00 m for a North – South wall and 2.66 m for an East – West wall. Since shaded areas have small surface

temperature (T_s) and appear to have a low reflectance, the expected relationship between reflectance and T_s is not preserved at shaded surfaces.

ATLAS calibration and correction is described by Rickman et al. (2000). From the spectral irradiance in each band [W cm^{-2} sr^{-1} μ^{-1}]the following quantities were computed. *NDVI* was calculated as in previous ATLAS studies (e.g. Lo et al., 1997) as:

$$NDVI = \frac{(b6-b3)}{(b6+b3)}. \quad (1)$$

Surface albedo was calculated as the ratio of incident irradiance that is reflected in the VNIR (bands 1-6). T_s was computed assuming an emissivity of 0.98. Since emissivities in an urban landscape varies from 0.91 to 0.99 (MODIS emissivity library), the surface temperatures used throughout this study should be considered as thermal energy expressed in temperature units. A calculation based on actual emissivity would increase T_s. Emissivity could be obtained at high resolution based on land cover class (Nichol 2009) or at low resolution through methods that utilize multiple TIR bands, e.g. the Grey Body Emissivity (Barducci and Pippi 1996) or Temperature Emissivity Separation methods (Kealy and Hook 1993). These calculations are left to future work.

ATLAS data were aggregated to 90 m resolution and to simulate ASTER satellite data. The original 10 m resolution data is used as the 'measured temperature' to evaluate the accuracy of the sharpening methods similarly as in Agam et al. (2008). *NDVI* and T_s were aggregated by averaging *NDVI* and TIR irradiance from the 10 m high resolution pixels, respectively.

Table 1: ATLAS bands and approximate band widths. Bands 3 and 6 are used for the NDVI calculation. Band 12 is used to calculate T_s.

ATLAS band	Approximate Bandwidth (μm)
1	0.45 – 0.52
2	0.52 – 0.60
3	0.60 – 0.63
4	0.63 – 0.69
5	0.69 – 0.76
6	0.76 – 0.90
7	1.55 – 1.75
8	2.08 – 2.35
9	3.35 – 4.20
10	8.20 – 8.60
11	8.60 – 9.00
12	9.00 – 9.40
13	9.60 – 10.2
14	10.2 – 11.2
15	11.2 – 12.2

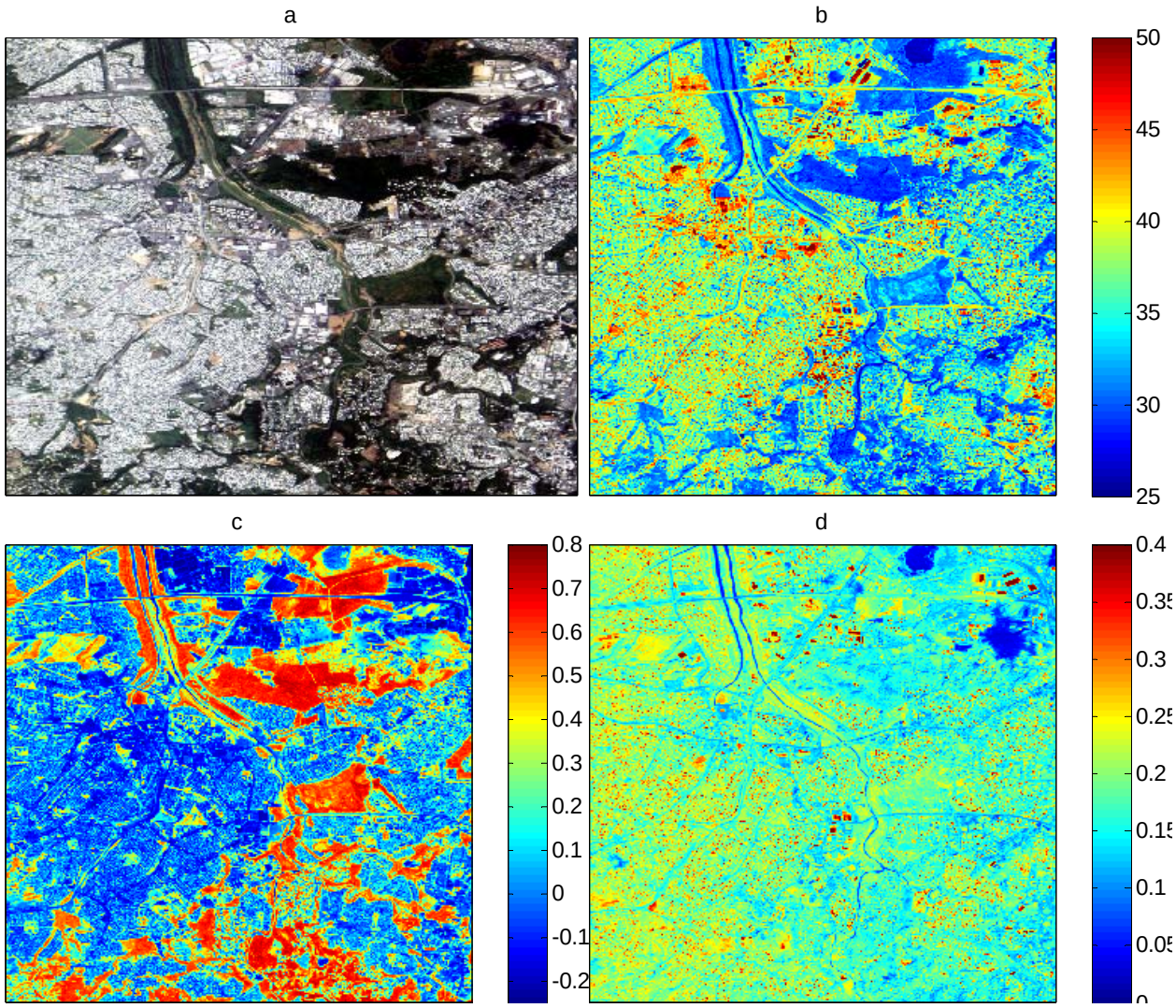

Figure 1: 9 x 7.2 km images of corrected and calibrated ATLAS ,measurements over a region of San Juan, Puerto Rico centered at 18.3933°N, 66.1447°W on February 16, 2004 from 1507-1512 AST. (a) visible composite image; (b) Surface Temperature; (c) NDVI; (d) albedo. The high albedo features in the northern region are commercial buildings. The large, white region in the West (Fig. 1a) is suburban residential. The high NDVI regions are densely vegetated. Rio Hondo river runs North-South from the top of the image.

3. Relationship between VNIR and TIR data

3.1 High resolution (10 m)

The assumption behind any thermal sharpening tool is that a relationship must exist between the TIR data and the visible and near-infrared (VNIR) data at the high resolution. Since all ATLAS

bands were acquired at 10 m resolution, this assumption could be tested by investigating the relationship between *NDVI*, α, and T_s (Fig. 2). Each 10 m pixel was sorted into one of 100 *NDVI* x 100 α bins, and the average T_s of each bin, along with the standard deviation and total number of pixels in the bin is displayed in Figure 2. This display format also allows visualization of the relationship of T_s to *NDVI* at any constant α or T_s to α at any constant *NDVI*. For example, consider the vertical dashed line in Fig. 2a at α = 0.2. Going from *NDVI* of 0.0 to 0.6, T_s decreases from about 40 to 30 ^{o}C. Fig. 2b shows the variance of the pixels along that same line to be less than 3 ^{o}C (i.e. much less than the observed change in average T_s), while Fig. 2c shows that the line is in a high density of samples, with over 100 samples contributing to each mean T_s and standard deviation pixel. Consequently, T_s decreases with *NDVI*, but the slope is different for different α.

Figure 2 shows that, a s expected, the highest T_s occur for -0.2 < *NDVI* < 0.0 and 0.1 < α < 0.25, which are typical properties of unvegetated, man-made urban materials. With increasing *NDVI*, T_s decreases as more vegetation leads to more latent heat flux and evaporative cooling. *NDVI* < -0.25 shows water bodies with low albedo and negative NDVI. Figure 2 also shows a strong dependence of T_s on α, which differs by *NDVI*. In the built up region (-0.2 < *NDVI* < 0.2) an increase in α leads to a decrease in T_s, as lighter surfaces reflect more solar radiation. Increasing α in the vegetative region (*NDVI* > 0.2) leads to an increase in T_s since darker vegetative areas tend to have denser and healthier (more transpiring) vegetation than drier, stressed vegetation. Overall, for the region with the greatest density of samples, a bivariate function T_s(*NDVI,α*) is required to fit the data with little scatter (small standard deviation of T_s in Fig. 2b*).* Since the

relationship between T_s, *NDVI* and α is nonlinear, higher order polynomials are required to describe it.

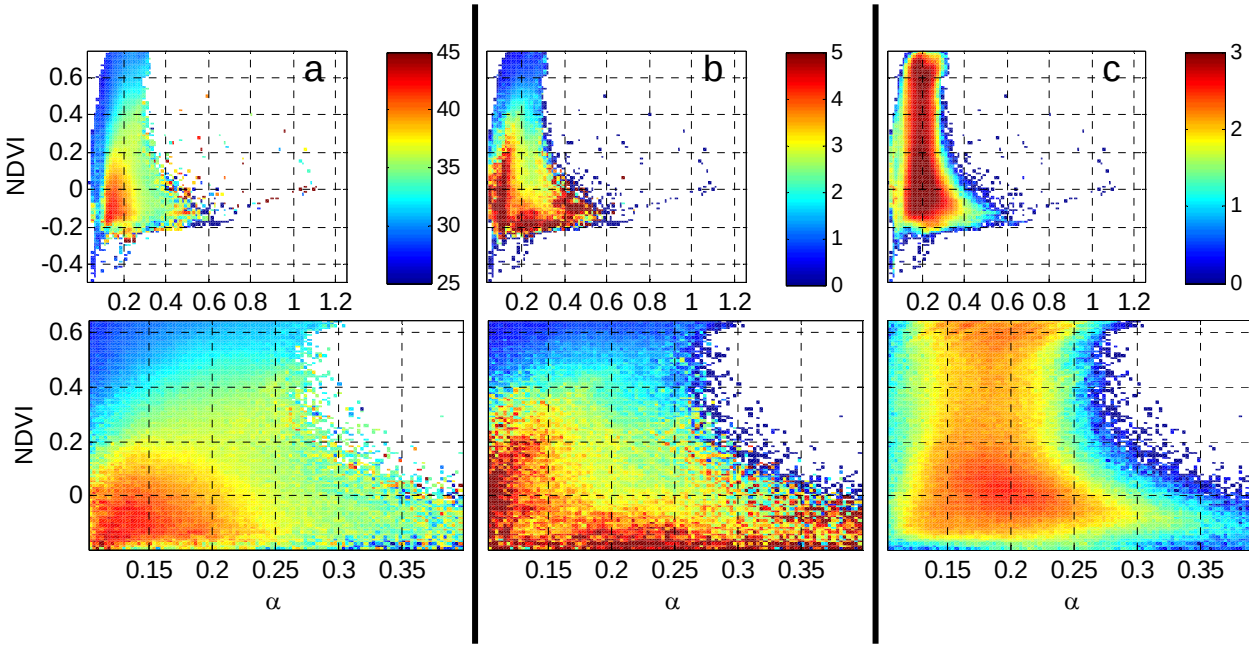

Figure 2: (a) Mean and (b) standard deviation of T_s [°C] and (c) histogram [$\log_{10}$(# of pixels)] vs. *NDVI* and albedo for (top) all data and (bottom) region with the majority of the data.

The relationships shown in Fig. 2 also reveal outliers with unrealistic values of $\alpha > 0.8$ and seemingly erroneous cases of high T_s and high albedo over rooftops. These albedo outliers may be due to roof coverings such as gravel that have non-lambertian reflectance characteristics.

3.2 Low resolution (90 m)

A strong relationship between T_s vs. *NDVI* and α exists at the 10 m resolution (Fig. 2). When applying sharpening techniques to satellite data, however, only low resolution T_s will be available for training this relationship. To test the assumption of scale-invariance, the relationship of T_s vs. *NDVI* and α were again compared at the low resolution (Figure 3). Though the low resolution data cover a smaller *NDVI* and α range than the high resolution data, the

NDVI relationship is consistent. The analysis in Section 3 motivates the development of the sharpening method, which consists of fitting a 4th order, bivariate $T_s(NDVI, \alpha)$ polynomial to the low resolution training data (Section 4.3). The aim of the model is to fit Fig. 3 to recreate the true relationship observed in Fig. 2a and use it to assign high resolution T_s. Assuming this can be done accurately, random errors in the sharpened temperatures will be due primarily to deviations shown in Fig. 2c.

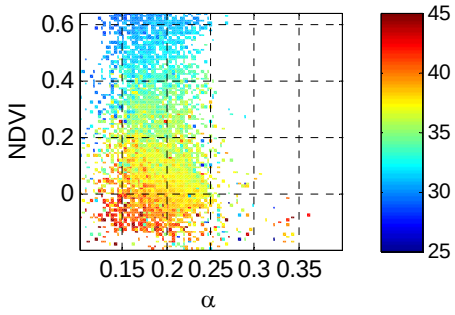

Figure 3: *NDVI* and *albedo* vs. T_s [°C] at the aggregated resolution of 90 m. Due to the low number of pixels, the majority of the bins contain less than 5 pixels, making histogram and standard deviation figures (as used in Fig. 2) irrelevant.

4. Sharpening Methodology

4.1 UniTrad

UniTrad is the base case, where the high resolution T_s is assumed to be uniform within the underlying low resolution pixel (Kustas, 2003).

4.2 TsHARP

169 The TsHARP method (Agam et al. 2007) is applied by calculating a simplified fractional
170 vegetation cover ($f_{cs90} = (1 - NDVI_{90})^{0.625}$) at the low 90 m resolution. A linear regression
171 between f_{cs90} and T_s at the low resolution yields the coefficients c_0 and c_1 in equation (2):

172 $$T_{s90} = c_0 + c_1 f_{cs90}. \quad (2)$$

173 Each high resolution pixel is then assigned a temperature based on the high resolution *NDVI*:

174 $$T_s = c_0 + c_1(1 - NDVI)^{0.625} + dT_s \quad (3)$$

175 and a difference $dT_s = T_{s90} - \hat{T}_{s90}$ which corrects for the difference in T_s between measured
176 T_{s90} and $\hat{T}_{s90}$, the mean value of the sharpened surface temperature within each low
177 resolution pixel. The addition of dT_s conserves energy within each low resolution pixel such
178 that aggregating the sharpened T_s reproduces the original low resolution T_{s90}.

179 *4.3 High resolution Urban Thermal Sharpener (HUTS)*

180 Four steps were defined that outline the approach to sharpening which are similar to the
181 procedure in TsHARP. Each step was individually optimized in the development of HUTS.

182 *Aggregation* consists of averaging *NDVI* and *α* over each low resolution pixel.

183 *Training* is conducted by applying multi-variate regression to solve for the vector **P** (**P** = [p_1 p_2 …
184 p_{15}]) of coefficients for the 4th order, bivariate regression of T_{s90} based on the 90 m resolution
185 *NDVI* and *α*.

186 *Sharpening* Is conducted by applying Eq. 4 to the *NDVI* and *α* of each high resolution pixel to
187 obtain the high resolution T_s:

$$T_s = p_1 NDVI^4 + p_2 NDVI^3 \alpha + p_3 NDVI^2 \alpha^2 + p_4 NDVI \alpha^3 + p_5 \alpha^4 + p_6 NDVI^3 + p_7 NDVI^2 \alpha + p_8 NDVI \alpha^2 + p_9 \alpha^3 + p_{10} NDVI^2 + p_{11} NDVI \alpha + p_{12} \alpha^2 + p_{13} NDVI + p_{14} \alpha + p_{15} \quad (4)$$

Quality control is then performed, as the regression is poorly fit outside of the region with a high density of data points. A reasonable temperature is defined as 27 ^{o}C < T_s < 60 ^{o}C, where the lower limit is set by the water surface temperature and the upper limit is 5 ^{o}C larger than the highest value of T_{s90}. If the temperature is outside the acceptable range, it is defined through an interpolation of the surrounding 5x5 pixel block weighted by distance. In the case that the surrounding 5x5 pixel block does not contain a pixel with an acceptable T_s, an iterative process is used until all pixels have been assigned a T_s. Finally, the sharpened pixel temperatures are corrected by applying the same energy balance procedure used for TsHARP. [An uncertainty weighted correction was also attempted, where the uncertainty metric was assigned to each pixel based on the variability of T_s within its range of *NDVI* and α and whether or not it was acquired through interpolation. The uncertainty was then used as a weighting factor where the pixels with the greatest uncertainty were changed the most to achieve energy balance. However, this method resulted in larger sharpening errors and was discarded.]

5. Results

5.1 Sharpened images and qualitative analysis

Figure 4 shows the measured 10 m T_s, the unsharpened 90 m image, and the sharpened image from both HUTS and TsHARP. Water pixels (from the rivers) can be ignored as they were

not taken into consideration when training the sharpening method, though the error in their estimation contributes to the error metrics in section 5.3. The improvement of both TsHARP and HUTS over UniTrad is evident in Fig. 4. Major landscape features such as parks are clearly delineated in TsHARP and HUTS. Small urban features such as roads which are barely visible in UniTrad become well resolved in TSHARP and HUTS. However, smaller urban features which cause variability at the high resolution (e.g. in and around the black box) are not depicted accurately. Consequently, the quality of sharpening of smaller urban features requires further investigation.

Figure 5 shows the same results zoomed into a mixed urban and suburban region. In the suburban areas (region A) HUTS accurately resolves the T_s patterns over roads, yards, and buildings, but not as distinctly as the measured T_s. TsHARP, however, inaccurately shows roads to be cooler than buildings since they have a higher NDVI. There are some regions where HUTS is visibly superior to TsHARP, but both do not resolve or represent microscale variability. Region B highlights a parking lot, where HUTS captures the variability between the lot and surrounding buildings that TsHARP does not. Region C highlights a boundary between an asphalt road and dirt to the North which is resolved by HUTS but not in TsHARP. Both TsHARP and HUTS do not represent the true variability of T_s which is a result of the averaging through the regression polynomial. There sometimes occur large gradients in T_s along the boundaries of the coarse pixels (e.g. north-west part of Fig. 5), which is a result of forcing energy conservation across the low resolution pixels. The very cold (very warm) 'outlier' high resolution pixels are overpredicted (underpredicted) by the sharpening polynomial leading to a erroneous decrease (increase) in temperature for all high resolution pixels once energy conservation is applied.

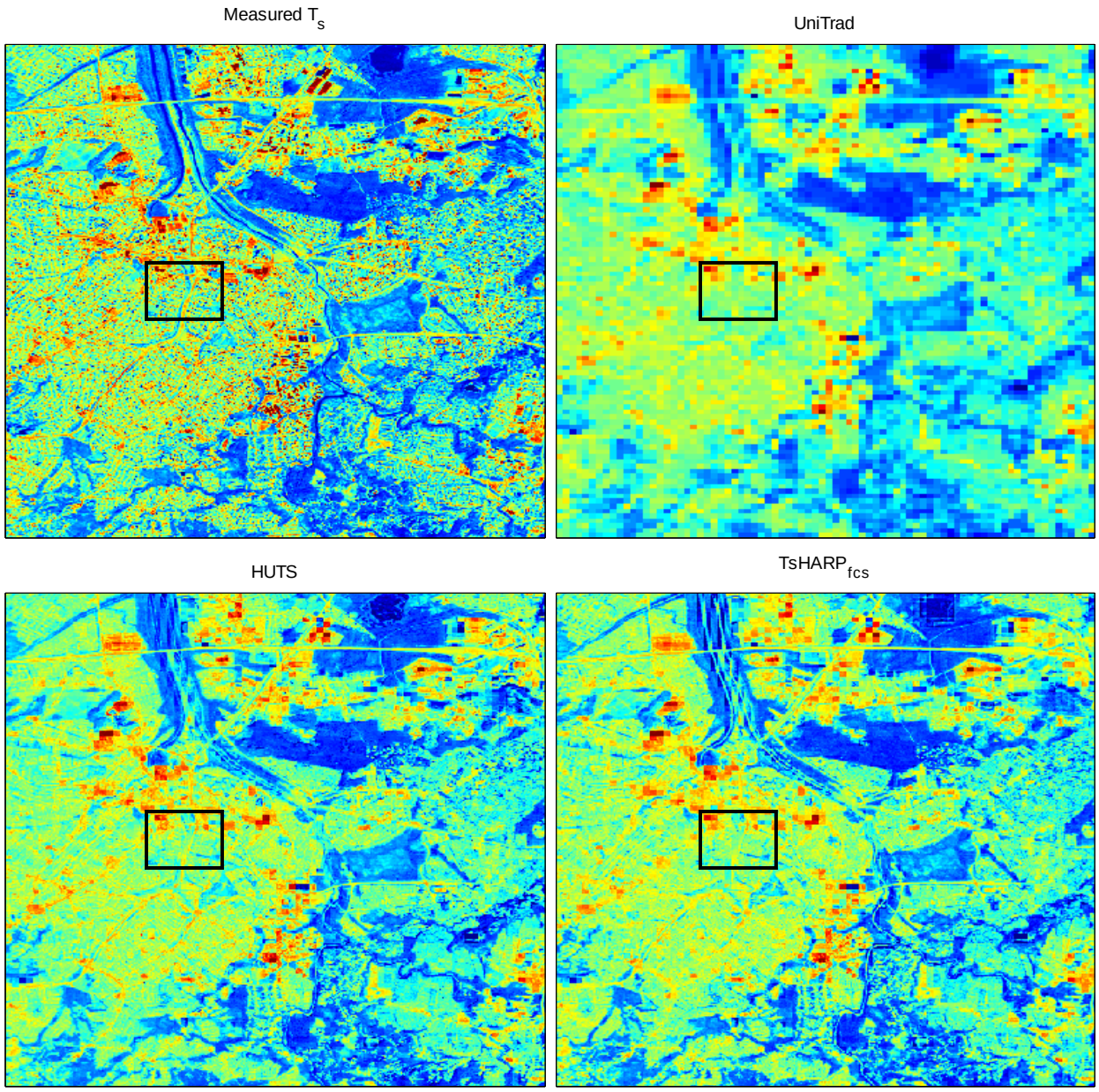

230

231 **Figure 4: T_s maps of the area shown in Fig. 1 including measured surface temperature at 10 m, unsharpened**
232 **surface temperature at 90 m (UniTrad), and sharpened temperature for both HUTS and TsHARP. The 900 x 720**
233 **pixel image covers a region of 9.0 x 7.2 km. Black boxes outline the close-up region shown in Fig. 5.**

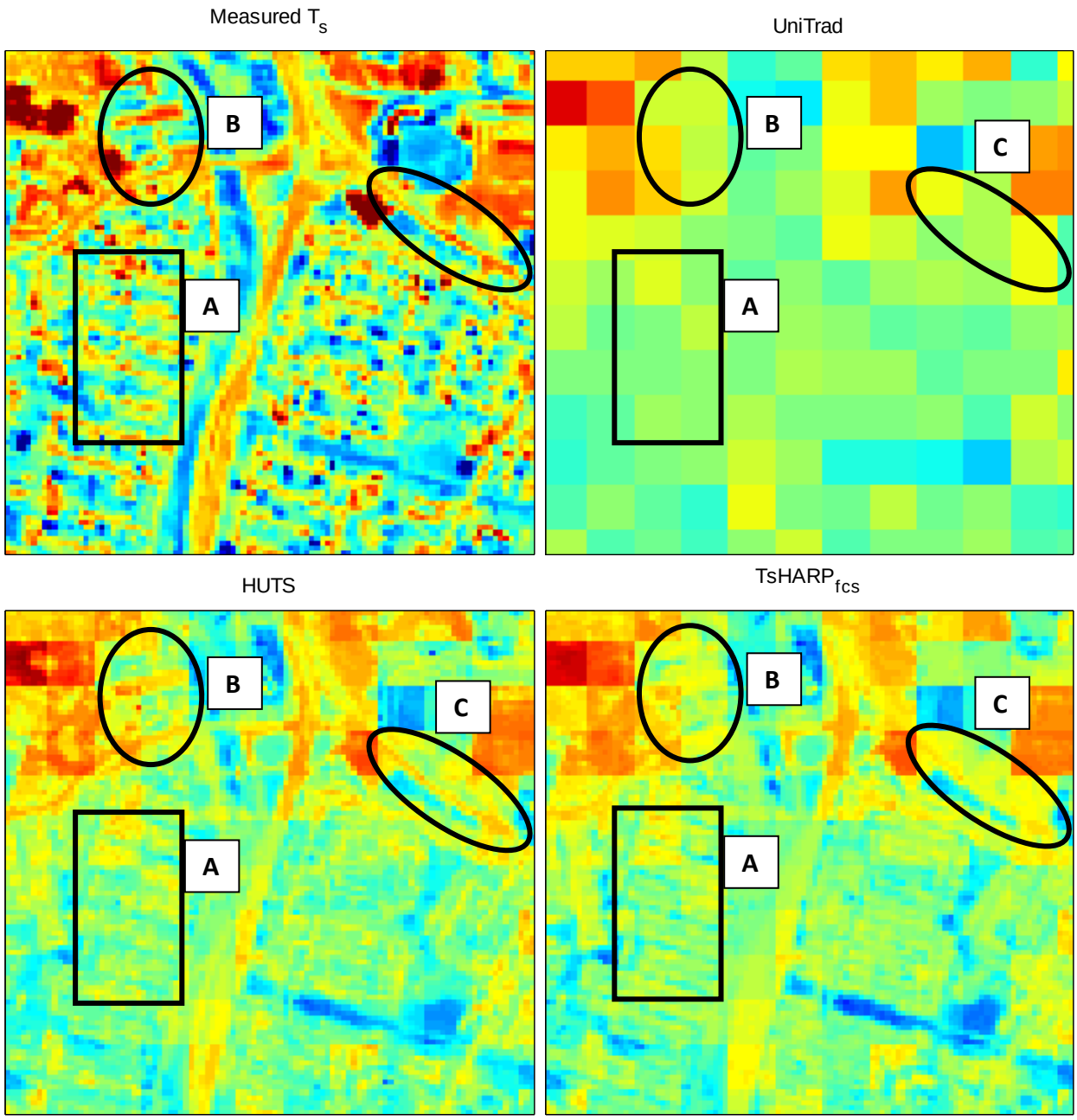

234

235 **Figure 5: Sharpened T_s zoomed in to a 100 x 100 pixel urban region (centered at 18.390698°N, 66.153084°W) at**
236 **10 m resolution. The figure shows a major highway intersection (Cll 2 and Carr 174). To the south of the east-**
237 **west highway are mostly residential neighborhoods with trees, while parks, parking lots, and commercial**
238 **buildings are to the north. West of the north-south highway is a waterway.**

239

240 *5.2 Distribution of sharpened T_s vs. NDVI and α*

The distribution of sharpened T_s stratified by *NDVI* and α is shown in Fig. 6 to determine how the relationships are represented after sharpening. Despite the limitations of the low resolution training set, HUTS recreates the high resolution relationship more accurately than TsHARP. Most of the differences are in regions of high T_s variability. There, the 4th order polynomial cannot resolve the differences in T_s or application of energy conservation over the low resolution pixel may result in erroneous corrections. Presumably other (unobserved) variables such as geometrical or physical properties of the urban fabric would have to be considered to explain the T_s variability. However, HUTS shows a decreases in error compared to TsHARP especially for the higher albedo for both vegetated (NDVI ~ 0.4) and urban pixels (NDVI ~ 0).

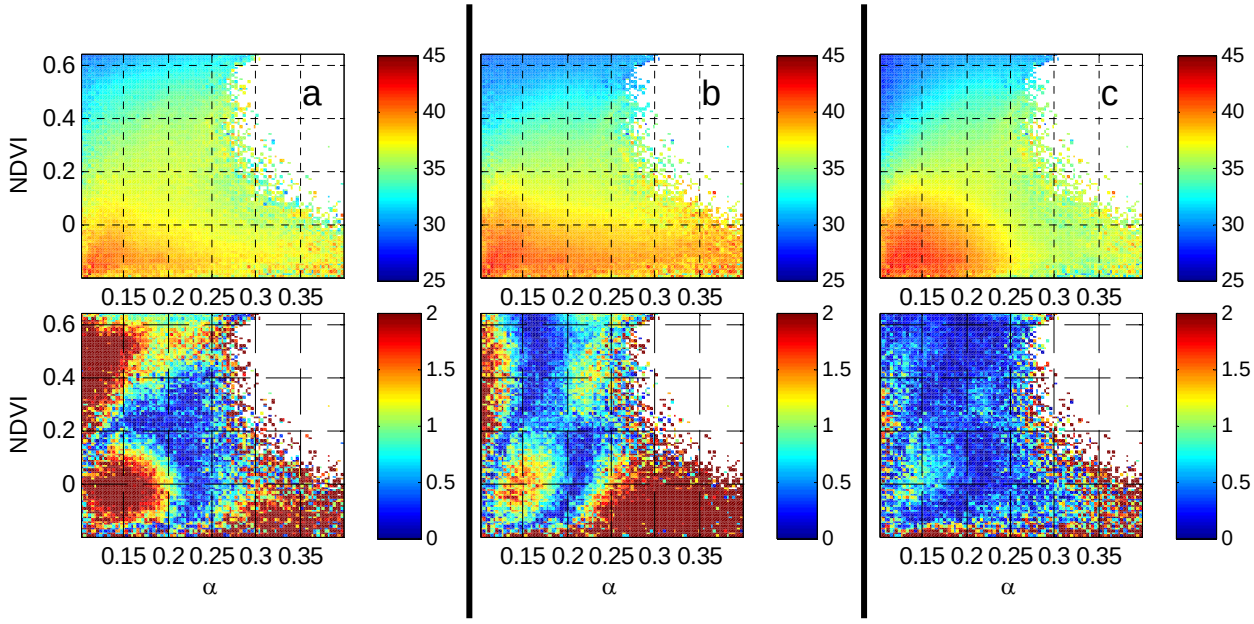

Figure 6: T_s vs *NDVI* and *α* for UniTrad (a), TsHARP (b), and HUTS (a) (top) and difference to measured T_s (bottom) in ^{o}C.

5.3 Error and correlation metrics and accuracy by land class

255 Root Mean Square Error (RMSE), Mean Absolute Error (MAE), and correlation coefficient (R)
256 were used to quantify the difference between sharpened and measured T_s at high resolution
257 for the entire 900 x 720 pixel image (Table 2). Over the entire image, HUTS improves upon
258 TsHARP about as much as TsHARP improves upon UniTrad for both error measures. Comparing
259 HUTS directly to UniTrad shows a 17% reduction in RMSE and 22% reduction in MAE.

260 **Table 2: Error in the estimation of sharpened T_s over the image in Fig. 4.**

Method	RMSE [K]	MAE [K]	R	MBE [K]
UniTrad	3.33	2.48	0.712	0.000
$TsHARP_{fcs}$	3.07	2.17	0.765	-0.019
HUTS	2.76	1.94	0.813	-0.015

261

262 Since HUTS is developed specifically for use in urban areas it is useful to examine its accuracy
263 within various land classes. For classification a training set was developed based on manual
264 selection of pixels and the classification function in MATLAB's image processing toolbox was
265 used on high resolution ATLAS bands 1, 2, 3, 5, 7, 8, as well as *NDVI* and α (Fig. 7).

266 The land classes used were motivated by Nichol (2009) and included 'Forest', 'Water', 'Dry
267 Grassland', 'Other Vegetation', 'Urban', and 'Soil/Sand'. However, 'Urban' was replaced by
268 'Suburban', 'Warehouse', 'Road', and 'Recreation'. The classification also contains a 'misfit'
269 class with pixels that were not highly matched with any class ('highly matched' = >80%
270 agreement with algorithm-defined parameters for any class).

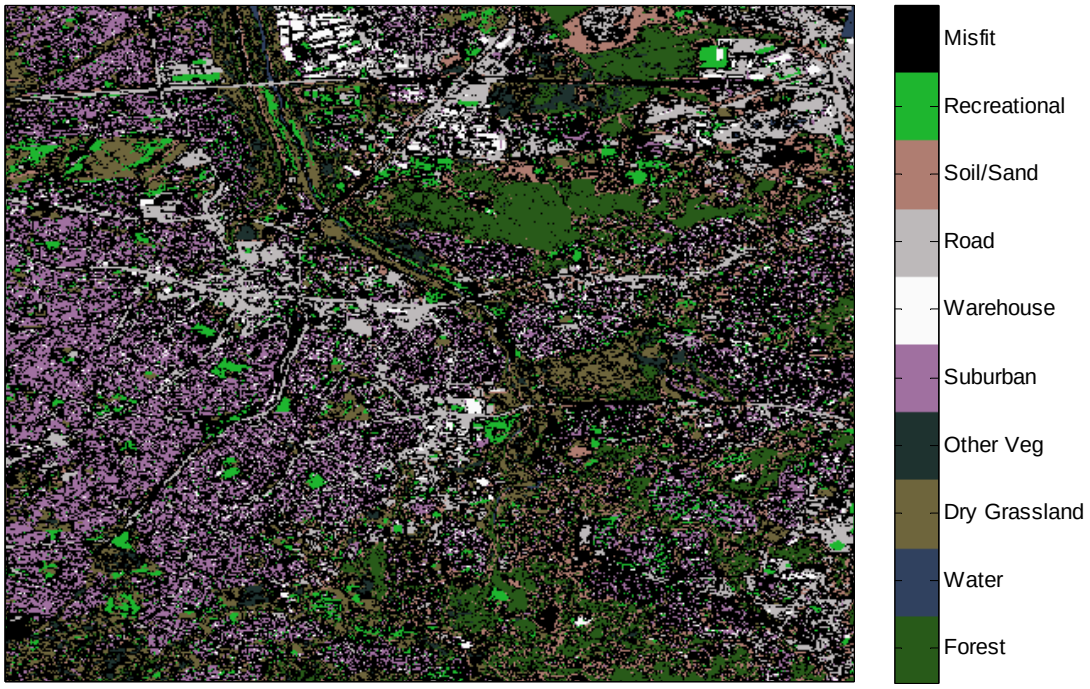

Figure 7: Scene (same as Fig. 4) with land cover classification into 9 classes. The class 'misfit' contains pixels with less than 80% fit to any category.

RMSE, MAE, mean bias error (MBE) and correlation coefficient were calculated within each land cover class (Figure 8). Since 'Other Vegetation' has a much lower number of pixels than the other classes, the result may not be significant. The high errors in 'warehouse' class are partially due to the high albedo 'outliers' observed in Fig. 2 which account for many pixels in the 'warehouse' class.

The 'suburban' class is poorly defined since at 10 m resolution it is a combination of landcover types. Instead of using the image processing toolbox to determine suburban pixels, the 'road', 'water', and 'recreational' pixels were excluded from a residential area of 200 x 200 pixels to form the suburban class. While the MBE for all methods in the suburban class is nearly zero, HUTS has a significantly higher correlation, meaning that it better captures the variability in

284 suburban LST caused by houses, yards, and mixed pixels. For the other land classes, HUTS
285 performs measurably better than both TsHARP and UniTrad, especially for classes defining
286 small scale features such as 'road' and 'soil/sand'.

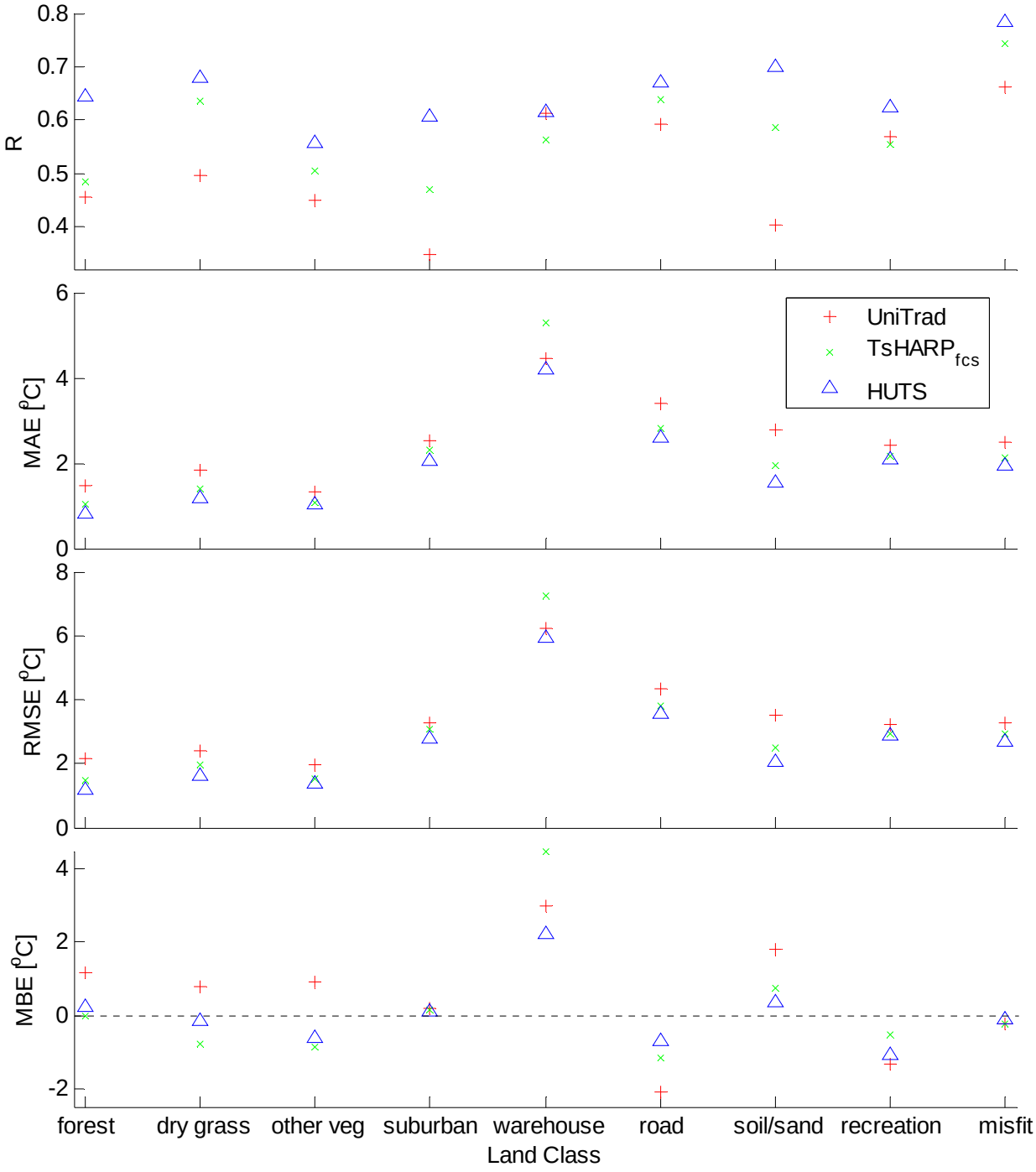

287

288 **Figure 8: Graphical representation of correlation coefficient, MAE, RMSE, and MBE in sharpened T_s by land class.**

6. Conclusions

Albedo and vegetation are expected to be important determinants of land surface temperatures (LST) in urban areas. The **High-resolution Urban Thermal Sharpener** (HUTS) method was motivated by analysis of the high resolution relationship between the TIR and VNIR signal (NDVI and albedo) from 10 m resolution ATLAS data over Puerto Rico. It was demonstrated that a low resolution (90 m) NDVI and albedo training set preserved the observed relationship to LST at high resolution. The training relationship was applied to estimate high resolution LST from 90 m LST sharpened using the VNIR signal at 10 m resolution over a 900 x 720 pixel image. Since HUTS can express the complex non-linear relationship between LST, albedo, and NDVI, it performed significantly better than both no sharpening (UniTrad) and an approach solely based on NDVI (TsHARP) based on qualitative comparison and RMSE, MAE, and correlation coefficient. Overall, HUTS showed an improvement of over 0.5 ^{o}C and over 17% in MAE and RMSE from no sharpening, more than twice the improvement from the TsHARP method. A land classification was applied to the image, and sharpening accuracy was assessed in each land class. The low MBE of HUTS indicated that the average LST of various land classes in the HUTS sharpened image is a more realistic input to models for urban microclimate or building energy use.

Since HUTS is a redistribution of LST based on assumed relationships, the source of error is twofold. The first is variance of high resolution LST at constant NDVI and albedo. This is quantified for the study area in Fig. 2b, and is less than 3 ^{o}C for the majority of the study area. The second source of error is from the ability to train the high resolution relationship from the

low resolution data. This is quantified for the study area in Fig. 6c, and is less than 0.75 ^{o}C for the majority of the study area. The assumed relationships are accurate, and the reallocation results in higher accuracy than other sharpening methods.

While HUTS was trained in the same *study area* that was used for validation, since the validation data (high resolution LST) is not used in the training this serves as an independent validation of HUTS. However, our study does not evaluate whether the relationship between Ts, NDVI and albedo is applicable across measurements platforms. While only a small area is presented in this manuscript, HUTS was applied to other regions of the dataset with similar results. Any other high resolution urban dataset could also be used for validation, and similar results are expected.

HUTS is proposed as a method for providing an estimate of the TIR signature at the same resolution as VNIR satellite data. Since it is based on physical parameters as opposed to lower level parameters (direct numerical (DN) value, radiance at sensor, etc), HUTS is applicable to calibrated datasets acquired from many remote sensing platforms. For example, HUTS can be applied to widely available ASTER images to estimate LST at the 15 m VNIR resolution from the measured 90 m TIR resolution. HUTS may also be applicable to lower resolution data such as that from MODIS, where it could increase thermal IR resolution from 1000 m to ~ 250m. While the MODIS resolution is too coarse to be of interest for many urban microclimate applications, TsHARP was found to be more accurate when sharpening to lower resolutions (Agam et al., 2008). In heterogeneous urban areas HUTS sharpened LST will provide more accurate input data for studies on how varied land classifications and land use (LCLU) affect the thermal

response of the urban fabric and the urban microclimate. The scale of heterogeneity in surface roughness impacts turbulent parameters such as blending height (Bou-Zeid and Parlange, 2007). Similarly, micro-scale heterogeneity in surface heat flux will impact flow and mixing in urban canyons (Castillo et al. 2009), and HUTS can provide measured high-resolution surface heat fluxes to input into simulations.

Acknowledgements

The collection of ATLAS data was partially sponsored by the NASA-EPSCoR program of the University of Puerto Rico, NASA's Summer Faculty Fellowship Program, the U.S. National Oceanic and Atmospheric Administration Cooperative Research Center of City College of New York City, and NASA's Global Hydrology and Climate Center, Huntsville, Alabama. This work was funded by a NASA GSRP Fellowship. Kleissl was supported by a NSF CAREER award.

Appendix A: **Sensitivity of HUTS**

Since various options exist for the implementation of HUTS, a brief justification on the implementation and sensitivity to different options is included here.

Using an entire flight path for training Eq. 4, covering mountains and natural vegetation as well as the urban area, made the sharpened T_s biased low and increased the RMSE and MAE by 0.1-0.2 ^{o}C. This could be a result of lower terrain or the urban surface heat island effect that heats urban surfaces compared to surrounding terrain with the same NDVI and albedo. A higher error associated with a larger training set indicates that there are competing land cover types of different T_s in the same *NDVI* and α ranges and that the relationships developed through this

study are not universal. Rather, the training should only be conducted for the urban area where the sharpening will be applied.

The training data was also used to generate a look-up table based on Fig. 3 to find the sharpened T_s and the regression (Eq. 4) was only used on empty bins. While this method had a significantly shorter computational time, the error measures increased by 10-20%. In addition, the order of the regression was varied from 3 – 6. The 4^{th} order regression was the most accurate, with RMSE and MAE within 0.05 ^{o}C for the other orders.

The 'reasonable range' of T_s was chosen with the river temperature as the lower limit (for many other urban areas an ocean temperature could be a good choice) and 5 ^{o}C higher than the maximum low resolution temperature as the upper limit. Varying these limits by 5 ^{o}C changed RMSE and MAE by less than 0.1 ^{o}C. Overall, while many aspects of HUTS can be changed, it proves to be robust over a reasonable range of parameters.

References

Agam, N. W., W.P. Kustas, M. C. Anderson, F. Li, C.M.U. Neale (2007). A vegetative index based technique for spatial sharpening of thermal imagery. *Remote Sensing of Environment 107* , 545-558.

Agam, N. W., W. P. Kustas, M. C. Anderson, F. Li, P. D. Colaizzi (2008). Utility of thermal image sharpening for monitoring field-scale evapotranspiration over rainfed and irrigated agricultural regions. *Geophysical Research Letters 35* .

370 Agam, N. W., W. P. Kustas, M. C. Anderson, F. Li, P. D. Colaizzi (2007). Utility of thermal
371 sharpening over Texas high plains irrigated agricultural field. *Journal of Geophysical Research,*
372 *Vol. 112* .

373 Barducci, A. and I. Pippi (1996). Temperature and emissivity retrieval from remotely sensed
374 images using the "grey body emissivity" method, *IEEE Transactions on Geoscience and Remote*
375 *Sensing*, 34:3 681-695.

376 Beniston, M. (2004). The 2003 heat wave in Europe: A shape of things to come? An analysis
377 based on Swiss climatological data and model simulations, *Geophysical Research Letters*, 31,
378 L02202

379 Bou-Zeid, E. and M. B. Parlange (2007). On the parameterization of surface roughness at
380 regional scales, *Journal of the Atmospheric Sciences*, 64, 216 – 227.

381 Castillo, M.C.L., M. Kanda, M.O. Letzel (2009). Heat Ventilation Efficiency of Urban Surfaces
382 Using Large-Eddy Simulation, *Annual Journal of Hydraulic Engineering*, *JSCE*, 53, 175-180

383 Crutzen, P. J. (2004). The growing urban heat and pollution ''island'' effect—impact on
384 chemistry and climate. *Atmospheric Environment*, 38, 3539–3540.

385 Di Sabatino S., Leo L.S., Hedquist B.C., Carter W., Fernando H.J.S. (2009). Results from the
386 Phoenix Urban Heat Island (UHI) experiment: effects at the local, neighbourhood and urban
387 scales. Geophysical Research Abstracts, Vol. 11, EGU2009-12778, 2009 EGU General Assembly

388 González, J. E., Luvall, J. C., Rickman, D., Comarazamy, D. E., Picón, A. J., Harmsen, E. W.,
389 Parsiani, H., Ramírez, N., Vázquez, R., Williams, R., Waide, R. B., Tepley, C. A., 2005. Urban heat
390 islands developing in coastal tropical cities. EOS Transactions, AGU 86, 42, pp. 397 & 403.
391 González, J. E., Luvall, J. C., Rickman, D., Comarazamy, D. E., Picón, A. J., 2006. Urban Heat
392 Island identification and climatological analysis in a coastal, tropical city: San Juan, Puerto Rico,
393 in: Q. Weng and D Quattrochi (Eds.), Urban Remote Sensing, CRC Press, Boca Raton, FL, pp. 223-
394 252.
395 Guo, L.J., and J. McMoore (1998). Pixel block intensity modulation: Adding spatial detail to TM
396 band 6 thermal imagery, *International Journal of Remote Sensing*, 19:2477-2491

397 Hung, T., D. Uchihama, S. Ochi, Y. Yasuoka (2006). Assessment with satellite data of the urban
398 heat island effects in Asian mega cities, *International Journal of Applied Earth Observation and*
399 *Geoinformation 8*, 34-48.

400 Kealy, P. S. and S. J. Hook (1993). Separating temperature and emissivity in thermal infrared
401 multispectral scanner data: implications for recovering land surface temperatures, *IEEE*
402 *Transactions on Geoscience and Remote Sensing*, 31:6 1155-1164.

403 Kustas, W. P., J.M. Norman, M.C. Anderson, A.N. French (2003). Estimating subpixel surface
404 temperatures and energy fluxes from the vegetation index -- radiometric temperature
405 relationship. *Remote Sensing of Environment 85* , 429-440.

406 Lebassi, B ., J. Gonzalez, D. Fabris, E. Maurer, N. Miller, C. Milesi, P. Switzer, R. Bornstein (2009).
407 Observed 1970-2005 Cooling of Summer Daytime Temperatures in Coastal California, *Journal of*
408 *Climate*, 22, 3558-3573.

409 Lo, C. P. , D.A. Quattrochi, J.C. Luvall (1997). Application of high-resolution thermal infrared
410 remote sensing and GIS to asses the urban heat island effect. *International Journal of Remote*
411 *Sensing* , 18:2, 287-304.

412 Nichol, J. (2009). An emissivity modulation method for spatial enhancement of thermal satellite
413 images in urban heat island analysis. *Photogrammetric Engineering & Remote Sensing Vol. 75* .

414 NWS Daily Summary courtesy of wunderground.com.
415 http://www.wunderground.com/history/airport/TJSJ/2004/2/16/DailyHistory.html?req_city=Sa
416 n+Juan&req_state=PR&req_statename=Puerto+Rico, accessed 9/3/2010.

417 Quattrochi, D. A., J. C. Luvall, D. L. Rickman, M. G. Estes, C. A. Laymon, B. F. Howell (2000). A
418 decision support information system for urban landscape management using thermal infrared
419 data, *Photogrammetric Engineering and Remote Sensing*, 66:10, 1195-1207.

420 Rickman, D. L., J. C. Luvall, S. Schiller (2000). An algorithm to atmospherically correct visible and
421 thermal airborne imagery, *Workshop on Multi/Hyperspectral Technology and Applications*,
422 Redstone Aresenal, Alabama.

423 Small C. (2006). Comparative analysis of urban reflectance and surface temperature, *Remote*
424 *Sensing of Environment* 104, 168-189.

425 Streutker, D. R. (2003). Satellite-measured growth of the urban heat island of Houston, Texas,
426 *Remote Sensing of Environment*, 85:3, 282-289.

427 Voogt, J. A., T.R. Oke (2003). Thermal remote sensing of urban climates, *Remote Sensing of*
428 *Environment*, 86, 370-384.

429 Wilson, J. S., M. Clay, E. Martin, D. Stuckey, K. Vedder-Risch (2003). Evaluating environmental
430 influences of zoning in urban ecosystems with remote sensing, *Remote Sensing of Environment*
431 *86*, 303-321.

432 Yaghoobian, N., J. Kleissl, E. S. Krayenhoff (2010). Modeling the Thermal Effects of Artificial Turf
433 on the Urban Environment, *Journal of Applied Meteorology and Climatology*, 49:3, 332-345